Enhancement of the linear polarization of coherent bremsstrahlung by collimation of the photon beam

F. Rambo,[1] J. Ahrens,[2] H.-J. Arends,[2] R. Beck,[2] G. Galler,[1] J. D. Kellie,[3] H.-P. Krahn,[2] A. Kraus,[1,*] U. Ludwig,[2] J. Peise,[2] A. Schmidt,[2] M. Schumacher,[1] F. Smend,[1,†] F. Wissmann,[1] and S. Wolf[1]

[1]*Zweites Physikalisches Institut, Universität Göttingen, D-37073 Göttingen, Germany*

[2]*Institut für Kernphysik, Universität Mainz, D-55099 Mainz, Germany*

[3]*Department of Physics and Astronomy, The University of Glasgow, Glasgow Gl2 8QQ, Scotland, United Kingdom*

(Received 4 December 1997)

A method is described to precisely predict the relative intensities and degrees of linear polarization of coherent bremsstrahlung from diamond crystals, taking into account the collimation of the photon beam and the lateral distribution and angular divergence of the electron beam in addition to the properties of the crystal. It is confirmed that the increase of the degree of linear polarization through collimation of the photon beam is a sizable effect. Compared to previous approaches considerable progress has been made in reproducing the experimentally observed relative intensities of collimated coherent bremsstrahlung, by taking into account the angular distribution of coherent bremsstrahlung in full detail. For the predicted degree of linear polarization agreement with experimental data from MAMI (Mainz) is obtained on a $\gtrsim 3\%$ level of precision. [S0556-2813(98)03207-5]

PACS number(s): 25.20.Lj, 24.70.+s, 29.27.Hj

I. INTRODUCTION

Linearly polarized photons produced via coherent bremsstrahlung in a diamond monocrystal are an important tool for intermediate-energy photonuclear and hadron physics. With the advent of high-duty-factor electron accelerators like MAMI in Mainz this technique has experienced a dramatic improvement since now it has become possible to combine the coherent bremsstrahlung technique with the tagging technique to produce quasimonochromatic photons [1]. The main advantages of this combination over previous techniques are as follows: (i) The intensity spectrum of secondary electrons can be measured on line with a high energy resolution (2 MeV channel width at MAMI) at a rate of typically 5×10^5 s^{-1} per channel. This allows one to measure intensity patterns which may be used to determine the exact orientation of the crystal [1] *in situ.* (ii) The intensity spectra of secondary electrons provided by the tagger are identical with the corresponding spectra of photons before entering the collimator. This means that these uncollimated photon spectra are known on an absolute scale with extremely good precision.

In an actual experiment the photon beam has to be collimated in order to avoid halos around the reaction target. In the case of collimation, only a fraction ϵ (named the tagging efficiency in the following) of the produced bremsstrahlung intensity is available for the experiment. The collimation angle Θ_c is normally chosen as a compromise between good collimation and high tagging efficiency ϵ and is typically of the order of one or two times the characteristic angle $\Theta_{BH}=1/E_0$ of incoherent bremsstrahlung production [2], where E_0 is the electron energy in units of m_0c^2. This characteristic angle Θ_{BH} is the polar angle of a cone around the beam axis containing roughly $\epsilon_{incoh}=50\%$ of the incoherent intensity. For $\Theta_c=2\Theta_{BH}$ the corresponding number is $\epsilon_{incoh}=80\%$. For the electron energy of MAMI ($E_0=855$ MeV) we have $\Theta_{BH}=0.6$ mrad.

Collimation requires an additional measurement of the tagging efficieny. This measurement is carried out with a photon detector positioned in the direct beam, which requires that even for a Pb glass detector the electron current has to be strongly reduced. Therefore, good statistical precision requires a considerable amount of beam time.

Tagging-efficiency measurements carried out routinely at MAMI have clearly shown that the relative intensities in the coherent-bremsstrahlung peaks strongly depend on the collimation of the photon beam. This effect was predicted by Mozley and DeWire [3] a long time ago and was already more or less clearly seen in previous experiments [4–7] as a narrowing of the peaks in the intensity distributions of coherent bremsstahlung. The origin of this effect is that coherent bremsstrahlung is more strongly forward peaked than incoherent bremsstrahlung. The coherent bremsstrahlung may be smeared out, if the angular divergence of the electron beam is large. However, with the high quality of the electron beam at MAMI the forward peaking remains strong and can be used to improve on the available degree of linear polarization, provided the process of coherent bremsstrahlung production and the influence of collimation and other external parameters on intensity and degree of linear polarization are well enough understood.

In general terms the understanding [1,3,8,9] of the collimation effect is along the following lines: Photons belonging to the high-energy discontinuity of a peak of coherent bremsstrahlung go in the direction of the primary electron. Therefore, this discontinuity and some lower-energy part of the peak of coherent bremsstrahlung are not influenced by colli-

*Present address: Philips Forschungslaboratorium, Aachen, Germany.

†Author to whom all correspondence should be addressed. Electronic address: smend@up200.dnet.gwdg.de

mation. With decreasing energy the photons are emitted at an increasing angle with respect to the direction of the primary electron. Therefore, a low-energy cutoff is expected in the distribution of collimated coherent bremsstrahlung with some rounding off from the beam divergence. However, this low-energy cutoff did not show up in the measured intensity spectra. Instead a smooth low-energy flank was observed. In order to understand these measured intensity spectra of collimated coherent bremsstrahlung in detail, we found it necessary to carry out a precise calculation of the angular distribution of coherent bremsstrahlung and to take into account the lateral extension and the divergence of the electron beam in great detail.

In parallel to the present theoretical investigation the first measurement of the degree of linear polarization of collimated coherent bremsstrahlung has been carried out making use of coherent π^0 photoproduction on ^{4}He in the Δ range as a linear polarimeter. A preliminary account of the experiment is given in Ref. [10]. The rather precise results of that experiment serve as a proof that our new calculations are capable of reproducing both the intensity distributions of coherent bremsstrahlung and the degree of linear polarization.

II. THEORY

A. Kinematics of incoherent and coherent bremsstrahlung

In this work we use natural units ($\hbar = m_0 = c = 1$) unless we quote quantities explicitly with their units. Only extremely relativistic energies are considered.

In the bremsstrahlung process an electron having energy E_0 and momentum $\boldsymbol{p}_0$ emits a photon with energy k and momentum $\boldsymbol{k}$ forming the angle Θ_k with $\boldsymbol{p}_0$. For convenience we introduce the fractional photon energy $x = k/E_0$. After emission, the electron has the energy E and the momentum $\boldsymbol{p}$ forming the angle Θ_e with $\boldsymbol{p}_0$. The recoil momentum $\boldsymbol{q} = \boldsymbol{p}_0 - \boldsymbol{p} - \boldsymbol{k}$ is transferred to a third partner in the bremsstrahlung process. It has components q_l and q_t parallel and perpendicular to $\boldsymbol{p}_0$, respectively. The quantity q_l has a minimum $\delta \equiv q_l^{\min} = p_0 - p - k$ for forward emission of both the electron and the photon. For this case $q_t = 0$.

The minimum of q_l is related to x via

$$q_l^{\min} = \delta(x) = \frac{x}{2E_0(1-x)}. \tag{1}$$

It is also possible to define a maximum of $q_l^{\max} \approx 2\delta(x)$ which, however, is not sharp. For q_t we find the lower limit $q_t^{\min} = 0$ and the upper limit $q_t^{\max} \approx 2x$ which is of the order of 1. In momentum space these limits define the ''pancake,'' i.e., a shallow volume which is normal to, and centered on, the $\boldsymbol{p}_0$ direction.

If the recoil is taken up by a free atom, each point of the pancake can be the end point of the recoil vector $\boldsymbol{q}$. The resulting photon spectrum is given by the Bethe-Heitler cross section [2]. Its angular distribution is almost independent of the photon energy. The characteristic angle $\Theta_{\mathrm{BH}} = 1/E_0$ has already been mentioned in the Introduction.

Incoherent bremsstrahlung is the sum of contributions of atoms acting independently. In the case of coherent bremsstrahlung on a monocrystal the recoil is taken up by the entire lattice, without creation or annihilation of a phonon.

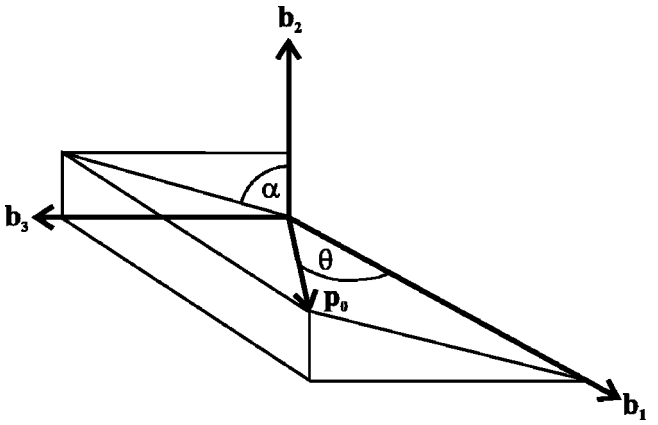

FIG. 1. Orientation of the crystal system $(\mathbf{b}_1, \mathbf{b}_2, \mathbf{b}_3)$ with respect to the momentum $\mathbf{p}_0$ of the incident electron. For more details see Fig. 11 in the Appendix.

For reviews of the theory, see, e.g. [11,12]. This process is possible only if the recoil vector $\boldsymbol{q}$ has its end point within the pancake and, at the same time, is identical to a vector $\boldsymbol{g}$ of the reciprocal lattice. The result is a peak in the photon spectrum whose upper limit is a discontinuity at

$$x_{\mathrm{d}} = \frac{2E_0\delta}{1+2E_0\delta}. \tag{2}$$

Bremsstrahlung from a monocrystalline radiator consists of both coherent and incoherent radiation. By suitably orienting the radiator with respect to the incident electron beam, one single recoil vector $\boldsymbol{g}$ can be selected to dominate the contributions to coherent bremsstrahlung in a selected range of x. In that region, then, the coherent part of bremsstrahlung shows strong linear polarization even if averaged over a solid angle having axial symmetry around $\boldsymbol{p}_0$. This is due to the fact that the recoil vector $\boldsymbol{g}$ is fixed in space, and defines a plane of reference for the electric vectors.

B. Orientation of the crystal

In order to describe the orientation of the crystal relative to the incident electron beam we introduce the following angles (cf. Fig. 1 and Tables I and II):

θ: angle between $\boldsymbol{p}_0$ and $\boldsymbol{b}_1$,

α: angle between the $(\boldsymbol{p}_0, \boldsymbol{b}_1)$ and the $(\boldsymbol{b}_1, \boldsymbol{b}_2)$ plane.

Here $\boldsymbol{b}_1$, $\boldsymbol{b}_2$, and $\boldsymbol{b}_3$ are the axes of the reciprocal lattice. Usually the planes $(\boldsymbol{b}_1, \boldsymbol{b}_2)$ and $(\boldsymbol{p}_0, \boldsymbol{b}_1)$ are called the crystal plane and the plane of incidence, respectively. For a given orientation, the longitudinal (l) and transverse (t) components of $\boldsymbol{g}$ with respect to the direction of $\boldsymbol{p}_0$ are, respectively,

$$g_l(\theta, \alpha) \approx g_1 + \theta(g_2 \cos\alpha + g_3 \sin\alpha), \tag{3}$$

$$g_t^2 \approx g_2^2 + g_3^2, \tag{4}$$

where θ is assumed to be small. The quantities g_1, g_2, g_3 are the components of $\boldsymbol{g}$ with respect to $\boldsymbol{b}_1, \boldsymbol{b}_2, \boldsymbol{b}_3$. Only those vectors of the reciprocal lattice lie in the pancake, for which

$$2\delta(x) \gtrsim g_1 \equiv q_1 \geqslant \delta(x). \tag{5}$$

The abrupt discontinuity at the high-energy side of the peak of coherent bremsstrahlung corresponds to the condition $g_1 = q_1^{\min} \equiv \delta(x)$, so that

$$x_d = \frac{2E_0 g_1}{1+2E_0 g_1} \tag{6}$$

is the fractional photon energy at the discontinuity. Strongly polarized coherent bremsstrahlung is produced if one single vector of the reciprocal lattice is in the pancake with its longitudinal component g_1 located close to the abrupt lower limit $\delta(x)$. For a cubic crystal like diamond the condition for obtaining a so-called single-point spectrum is $\theta \approx 60$ mrad, $\alpha \neq n(\pi/4)$. More details concerning these conditions are discussed in our previous paper [1].

In order to choose the reference plane for the polarization conveniently, we define an additional angle:

φ: angle between the $(\boldsymbol{b}_1, \boldsymbol{e})$ and the $(\boldsymbol{b}_1, \boldsymbol{b}_2)$ plane,

i.e., between the reference plane for the polarization of the photon and the crystal plane. It is convenient to have the reference vector $\boldsymbol{e}$ for the polarization orthogonal to $\boldsymbol{p}_0$ and in the horizontal plane of the laboratory, e.g., $\mathbf{e} = \mathbf{e}_x$. Since θ is small, $\boldsymbol{p}_0$ and $\boldsymbol{b}_1$ are almost parallel to each other, and the reference plane $(\boldsymbol{b}_1, \boldsymbol{e}_x)$ is, to a good approximation, horizontal.

III. DIFFERENTIAL CROSS SECTION FOR COHERENT AND INCOHERENT BREMSSTRAHLUNG

May [13] has calculated the differential cross sections for bremsstrahlung with linear polarization parallel and perpendicular to the plane of emission $(\boldsymbol{p}_0, \boldsymbol{k})$, respectively. Barbiellini *et al.* [14] applied their results to the calculation of coherent bremsstrahlung in monocrystals. In the present work we use their cross sections written differentially in energy and in the angles which define the direction of the emitted photon.

The differential cross section is the sum of a coherent part $d^3\sigma^{(c)}$ and an incoherent part $d^3\sigma^{(i)}$. The coherent part of the differential cross section consists of two contributions $d^3\sigma_\perp^{(c)}$ and $d^3\sigma_\parallel^{(c)}$ having their respective planes of linear polarization perpendicular and parallel to a plane of reference $(\boldsymbol{k}, \boldsymbol{e}_x)$, i.e., $d^3\sigma^{(c)} = d^3\sigma_\perp^{(c)} + d^3\sigma_\parallel^{(c)}$. Since in our experimental setup θ and Θ_k are both small, we can choose $(\boldsymbol{b}_1, \boldsymbol{e}_x)$ as a reference plane instead. The incoherent part shows no polarization under the present experimental conditions where only the photon beam is observed and averaged over a solid angle having axial symmetry around $\boldsymbol{p}_0$. Hence, the degree of linear polarization with respect to that plane is given by

$$P = \frac{d^3\sigma_\perp^{(c)} - d^3\sigma_\parallel^{(c)}}{d^3\sigma_\perp^{(c)} + d^3\sigma_\parallel^{(c)} + d^3\sigma^{(i)}}. \tag{7}$$

The coherent part of the differential cross section is written as

$$\frac{k}{\bar{\sigma}N}\left(d^3\sigma_\perp^{(c)} + d^3\sigma_\parallel^{(c)}\right) = \{[1+(1-x)^2]\Phi_1(\delta,\theta,\alpha) - \tfrac{2}{3}(1-x)\Phi_2(\psi_1,\delta,\theta,\alpha)\} \times \partial[U^2(\psi_1) - U^2]\, dU^2 d\psi_1 dk \tag{8}$$

and

$$\frac{k}{\bar{\sigma}N}\left(d^3\sigma_\perp^{(c)} - d^3\sigma_\parallel^{(c)}\right) = 2(1-x)\Phi_4(\psi_1,\delta,\theta,\alpha)\partial[U^2(\psi_1) - U^2]\, dU^2 d\psi_1 dk. \tag{9}$$

Here, N is the total number of atoms exposed to the electron beam, $\bar{\sigma} = (Z\alpha)^2$, ∂ is Dirac's delta function, and $U = \Theta_k E_0$ is the photon emission angle in units of Θ_{BH}. θ, α, and φ have been defined above, and ψ_1 is the angle between the planes $(\boldsymbol{k}, \boldsymbol{p}_0)$ and $(\boldsymbol{b}_1, \boldsymbol{p}_0)$, i.e., the azimuthal angle of the photon direction with respect to the plane of incidence (cf. Tables I and II). The functions Φ_1, Φ_2, and Φ_4 are defined in the Appendix.

Having chosen (i) the vector $\boldsymbol{g}$ in the reciprocal lattice, (ii) the orientation angles θ and α of the crystal, and (iii) the photon energy x, the polar emission angle U of the photon depends only weakly on ψ_1:

$$U(\psi_1) \approx \Gamma(\psi_1,\alpha) + \sqrt{\frac{g_1(\theta,\alpha)}{\delta} - 1 + \Gamma^2(\psi_1,\alpha)}, \tag{10}$$

where an additional term $-g_t^2/x$ in the radicand has been neglected. $\Gamma(\psi_1,\alpha)$ is defined in the Appendix.

The vector sum $\boldsymbol{k} + \boldsymbol{p}_1$ starts from the point $\boldsymbol{g}$ in momentum space. Therefore, the momentum $\boldsymbol{k}$ of a photon of coherent bremsstrahlung lies on a cone whose axis, in general, is not parallel to $\boldsymbol{p}_0$ but slightly tilted with respect to the latter. This is the reason for the weak dependence of the polar angle U on ψ_1.

Since the angular distribution of incoherent bremsstrahlung is almost independent of the photon energy, it can be factored out of the incoherent part $d^3\sigma^{(i)}$ of the differential cross section:

$$d^3\sigma^{(i)} \approx d\sigma^{(i)} \text{const} \times \frac{U dU d\omega}{(1+U^2)^2} \approx d\sigma^{(i)} f(U) U\, dU\, d\omega, \tag{11}$$

with

$$f(U) = [\pi(A_1 s_1^2 + A_2 s_2^2)]^{-1} \sum_{i=1}^{2} A_i \exp(-U^2/s_i^2), \tag{12}$$

where ω is the azimuthal angle of emission with respect to an arbitrary plane of reference, e.g., the horizontal plane of the laboratory. The second expression in Eq. (11) is a computationally convenient fit to the first one with parameters $A_1 = 0.7$, $A_2 = 0.3$, $s_1 = 0.637$, and $s_2 = 1.41$. $d\sigma^{(i)}$ denotes the incoherent part of the cross section given by [2]

$$\frac{k}{\overline{\sigma N}} d\sigma^{(\mathrm{i})} = \left\{ [1+(1-x)^2][\Psi_1^{(\mathrm{i})}(\delta) + \Psi_1^e] - \frac{2}{3}(1-x)[\Psi_2^{(\mathrm{i})}(\delta) + \Psi_2^e] \right\} dk. \quad (13)$$

The Ψ symbols of Eq. (13) are defined in the Appendix. The integration of $d^3\sigma_\perp^{(\mathrm{c})} + d^3\sigma_\parallel^{(\mathrm{c})}$ and $d^3\sigma_\perp^{(\mathrm{c})} - d^3\sigma_\parallel^{(\mathrm{c})}$ given in Eqs. (8) and (9) yields the single differential expressions [11]

$$\frac{k}{\overline{\sigma N}} (d\sigma_\perp^{(\mathrm{c})} + d\sigma_\parallel^{(\mathrm{c})}) = \left\{ [1+(1-x)^2]\Psi_1^{(\mathrm{c})}(\delta,\theta,\alpha) - \frac{2}{3}(1-x)\Psi_2^{(\mathrm{c})}(\delta,\theta,\alpha) \right\} dk, \quad (14)$$

$$\frac{k}{\overline{\sigma N}} (d\sigma_\perp^{(\mathrm{c})} - d\sigma_\parallel^{(\mathrm{c})}) = 2(1-x)\Psi_3^{(\mathrm{c})}(\delta,\theta,\alpha) dk. \quad (15)$$

Again, the Ψ functions are defined in the Appendix.

For the following discussions and comparisons with experimental data it is useful to define the relative cross sections $d^3\sigma/d^3\sigma^{(\mathrm{i})}$ and $d\sigma/d\sigma^{(\mathrm{i})}$, i.e., to normalize to the incoherent contribution. The quantity $kd\sigma(k)/dk$ usually is called the intensity, with the relative intensity defined accordingly.

IV. COLLIMATION OF THE PHOTON BEAM

Following the suggestion by Mozley and DeWire [3] a collimator is placed on the axis of the photon beam. The collimator is assumed to be circular, centered on the $\mathbf{p}_0$ axis, and to transmit only photons with $\Theta_k \leqslant \Theta_\mathrm{c}$. For a comprehensive review of the investigations done so far on this effect we refer, e.g., to [12] and references therein. First, we discuss bremsstrahlung produced by an ideal electron beam having zero divergence and zero diameter and neglect electron scattering in the radiator. In a good approximation we can further neglect the weak dependence of the polar angle U of the coherent radiation on ψ_1 and use

$$U = \sqrt{\frac{g_1(\theta,\alpha)}{\delta} - 1} \quad (16)$$

instead of Eq. (10). We can interpret the latter expression in the following way: While the angular distribution of the incoherent radiation does not depend on photon energy and can approximately be described as the sum of two Gaussians, the coherent radiation for a given reciprocal vector $\boldsymbol{g}$ is emitted into a fixed polar angle, which is the smaller the closer the lower boundary of the pancake moves to $\boldsymbol{g}$. Hence, for a given vector $\boldsymbol{g}$ the upper limit $U_\mathrm{c} = E_0\Theta_\mathrm{c}$ for the emission angle U sets a lower limit to the fractional energy of coherent bremsstrahlung, viz.,

$$x_\mathrm{c} = \frac{x_d}{1 + U_\mathrm{c}^2(1+x_d)}. \quad (17)$$

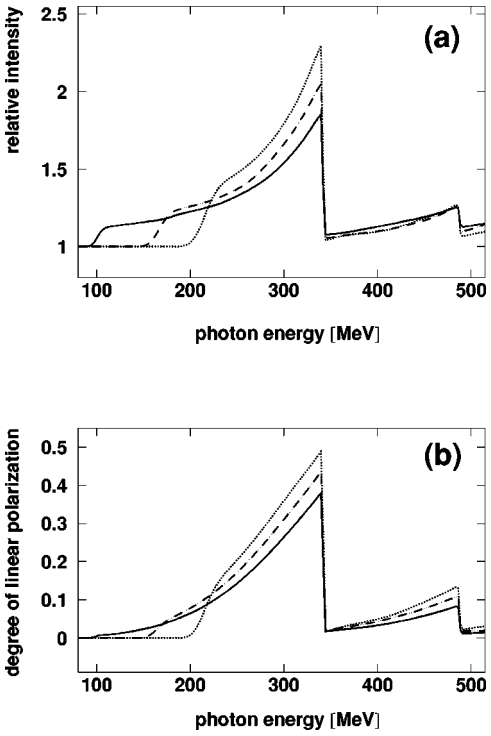

FIG. 2. Spectra of relative intensity (a) and degree of linear polarization (b) for different collimating angles: $\Theta_\mathrm{c} = 0.6$ mrad (dotted lines), 0.8 mrad (dashed lines), and 1.2 mrad (solid lines). The electron energy is $E_0 = 855$ MeV, and the orientation angles of the radiator are $\Theta = 63.3$ mrad and $\alpha = 620$ mrad, placing the discontinuity for the reciprocal vector $\mathbf{g} = [02\bar{2}]$ in the photon spectrum at $k_\mathrm{d} = 342$ MeV. The radiator is at room temperature ($T = 295$ K). The calculations have been performed for a radiator of thickness $d = 0.01$ mm and an almost ideal electron beam having the parameters $\sigma_x = \sigma_y = 0.1$ μm and $\sigma_{p_x}/E_0 = \sigma_{p_y}/E_0 = 0.01$ μrad.

On the other hand, the spectrum of incoherent bremsstrahlung is reduced by the factor

$$f_\mathrm{c} = \frac{U_\mathrm{c}^2}{1 + U_\mathrm{c}^2}. \quad (18)$$

This reduction of incoherent bremsstrahlung leads to an enhancement of the degree of linear polarization as illustrated in Fig. 2(b) for an example with three different angles of collimation.

Under experimental conditions we have to consider the (i) divergence and spatial extension of the electron beam, (ii) multiple scattering of electrons, and (iii) mosaic structure of the radiator crystal. Of the quantities which depend on the actual direction of the radiating electron the polar emission angle U and the lower boundary $\delta(x)$ of the pancake are the most important ones. Not only the directional distribution of the coherent bremsstrahlung is smeared out but also the lower and upper limits of the photon energy interval, viz., x_c and x_d, for the contribution of a given reciprocal lattice vector $\boldsymbol{g}$.

In order to describe the divergence of the incident electron beam $\boldsymbol{p}_0$ now denotes the beam axis, whereas $\boldsymbol{p}^* = \boldsymbol{p}_\parallel + \boldsymbol{p}_\perp$ is the actual momentum of a single electron having components $\boldsymbol{p}_\parallel$ and $\boldsymbol{p}_\perp (\ll \boldsymbol{p}_\parallel)$ parallel and perpendicular to

$\boldsymbol{p}_0$, respectively. We assume all the electrons to have the same energy and $\boldsymbol{p}_\perp$ to be distributed according to a two-dimensional Gaussian:

$$P(\chi,\lambda)\chi\, d\chi\, d\lambda = \frac{1}{2\pi\sigma_{p_x}\sigma_{p_y}}\, \exp\left(-\frac{\chi^2\cos^2\lambda}{2\sigma_{p_x}^2} - \frac{\chi^2\sin^2\lambda}{2\sigma_{p_y}^2}\right)\chi\, d\chi\, d\lambda. \tag{19}$$

Here $\chi = p_\perp$ is the polar angle between $\boldsymbol{p}_0$ and $\boldsymbol{p}^*$ in units of Θ_{BH} and λ the azimuthal angle between the divergence plane $(\boldsymbol{p}^*,\boldsymbol{p}_0)$ and the horizontal plane $(\boldsymbol{p}_0,\boldsymbol{e}_x)$ of the laboratory. The standard deviations σ_{p_x} and σ_{p_y} parametrize the horizontal and vertical divergences of the electron beam, respectively, in units of Θ_{BH}.

We assume the spatial extension of the beam to have a Gaussian distribution as well. The probability for an electron for hitting the radiator with the lateral displacement $\boldsymbol{r} = (\xi,\eta)$ with respect to the intersection of the axis of the electron beam and the radiator is then given by

$$K(\xi,\eta)d\xi\, d\eta = \frac{1}{2\pi\sigma_x\sigma_y}\, \exp\left(-\frac{\xi^2}{2\sigma_x^2} - \frac{\eta^2}{2\sigma_y^2}\right) d\xi\, d\eta. \tag{20}$$

Again, the standard deviations σ_x and σ_y parametrize the spatial dimensions of the electron beam in the horizontal and vertical directions, respectively.

Molière's theory of multiple scattering (see, e.g., [15]) predicts the directional distribution of an initially ideal beam of electrons after traversing a distance s in the radiator. For the purpose of the present work the Molière distribution may be approximated by a Gaussian distribution of the polar angles χ (expressed in units of $1/E_0$):

$$M_s(\chi)\chi\, d\chi = \frac{2}{\sigma_{\mathrm{Mol}}^2(s)}\, \exp\left(-\frac{\chi^2}{\sigma_{\mathrm{Mol}}^2(s)}\right)\chi\, d\chi. \tag{21}$$

For the calculation of the standard deviation $\sigma_{\mathrm{Mol}}(s)$ see Ref. [15]. In the case of carbon and $E_0 = 855$ MeV Molière's theory is valid for $s \gtrsim 8$ μm; in our experiments we used a diamond radiator of thickness $d = 100$ μm. Since the electron may radiate anywhere along its path through the radiator, the standard deviation σ_{Mol} has to be averaged to

$$\overline{\sigma}_{\mathrm{Mol}} = \frac{1}{d}\int_0^d \sigma_{\mathrm{Mol}}(s)ds. \tag{22}$$

The resulting distribution for $\boldsymbol{p}_\perp$ is obtained by convolution of the distributions (19) and (21):

$$P_{\mathrm{res}}(\chi,\lambda)\chi\, d\chi\, d\lambda = \frac{1}{2\pi\sigma_1\sigma_2}\, \exp\left(-\frac{\chi^2\cos^2\lambda}{2\sigma_1^2} - \frac{\chi^2\sin^2\lambda}{2\sigma_2^2}\right)\chi\, d\chi\, d\lambda, \tag{23}$$

with the standard deviations σ_1 and σ_2 given by

$$\sigma_{1(2)}^2 = \sigma_{p_{x(y)}}^2 + \frac{\overline{\sigma}_{\mathrm{Mol}}^2}{2}. \tag{24}$$

The effects of a possible mosaic structure are smaller than those of the beam divergence and are incorporated in an effective beam divergence which is an adjustable parameter.

A. Influence of photon collimation on incoherent bremsstrahlung

For incoherent radiation it is straightforward to modify the differential cross section given in Eq. (11) to take beam divergence and multiple scattering of electrons into account. We only have to transform Eqs. (12) and (23) into Cartesian coordinates in the laboratory and perform a convolution. The result is

$$f^*(U_x,U_y)dU_xdU_y = \frac{1}{4\pi\mathcal{N}}\sum_{i=1}^{2} A_i\frac{s_i^2}{\sigma_{i1}\sigma_{i2}}\, \exp\left(-\frac{U_x^2}{2\sigma_{i1}^2} - \frac{U_y^2}{2\sigma_{i2}^2}\right) dU_xdU_y, \tag{25}$$

where the standard deviations are given by

$$\sigma_{ij}^2 = \sigma_i^2 + \frac{s_j^2}{2}, \quad i,j = 1,2. \tag{26}$$

A photon emitted with polar angles (U_x,U_y) will hit the collimator at a point

$$\boldsymbol{r}_\gamma = \frac{l}{E_0}(U_x,U_y) + \boldsymbol{r} \tag{27}$$

in the plane perpendicular to the beam axis, where l denotes the distance between radiator and collimator and, as defined above, $\boldsymbol{r} = (\xi,\eta)$ is the lateral displacement of the electron in the radiator, with respect to the beam axis. Hence, under experimental conditions a collimator with radius R will reduce the incoherent radiation by the factor

$$f_{\mathrm{c}}(R) = \int_{r_\gamma \le R} K(\xi,\eta)f^*(U_x,U_y)dU_xdU_yd\xi d\eta. \tag{28}$$

B. Influence of photon collimation on coherent bremsstrahlung

The differential cross section for coherent radiation depends strongly on the orientation of the crystal with respect to the incident electron. Therefore, the geometry has to be analyzed carefully. For this purpose we have to introduce two additional azimuthal angles:

λ': angle between the $(\boldsymbol{p}_0,\boldsymbol{p}^*)$ and the $(\boldsymbol{p}_0,\boldsymbol{b}_1)$ plane,

κ: angle between the $(\boldsymbol{p}_0,\boldsymbol{b}_1)$ and the $(\boldsymbol{p}_0,\boldsymbol{e}_x)$ plane.

As all polar angles are small, we have $\lambda = \lambda' + \kappa$ and, to a good approximation, $\varphi = \alpha + \kappa$. Since an incident electron has the individual momentum vector $\boldsymbol{p}^*$, we have to define angles describing orientation of the crystal and emission of photons with respect to $\boldsymbol{p}^*$ instead of the beam axis $\boldsymbol{p}_0$, and

we shall mark the newly defined angles by an asterisk. Hence, in the formulas for coherent radiation we have to consider the following replacements:

$$\alpha \rightsquigarrow \alpha^*(\chi,\lambda'), \quad \psi_1 \rightsquigarrow \psi_1^*,$$

$$\theta \rightsquigarrow \theta^*(\chi,\lambda'), \quad U(\psi_1) \rightsquigarrow U^*(\psi_1^*,\chi,\lambda').$$

Using $\vartheta := E_0\theta$ and $\vartheta^*(\chi,\lambda') := E_0\theta^*(\chi,\lambda')$ as long as $\chi \leqslant \vartheta$, we have

$$\vartheta^*(\chi,\lambda') = \sqrt{\vartheta^2+\chi^2-2\vartheta\chi\cos\lambda'}, \tag{29}$$

$$\alpha - \alpha^*(\chi,\lambda') = \arcsin\frac{\chi\sin\lambda'}{\vartheta^*(\chi,\lambda')}. \tag{30}$$

Having made these replacements we denote the differential cross sections obtained in analogy to Eqs. (8) and (9) in the following way:

$$d^2\sigma_\perp^{(c)}(\chi,\lambda') + d^2\sigma_\parallel^{(c)}(\chi,\lambda'), \tag{31}$$

$$d^2\sigma_\perp^{(c)}(\chi,\lambda') - d^2\sigma_\parallel^{(c)}(\chi,\lambda'). \tag{32}$$

It should be kept in mind that these cross sections are differential only in k and ψ_1^* and that

$$U^*(\psi_1^*,\chi,\lambda') = \Gamma(\psi_1^*,\alpha^*(\chi,\lambda')) + \sqrt{\frac{g_1(\theta^*(\chi,\lambda'),\alpha^*(\chi,\lambda'))}{\delta} - 1 + \Gamma^2(\psi_1^*,\alpha^*(\chi,\lambda'))}. \tag{33}$$

As we did for incoherent radiation we use a coordinate system in the plane perpendicular to the beam axis with its origin at the center of the collimator and its axes horizontal and vertical in the laboratory, respectively. In this coordinate system (see Fig. 3) the vector $\boldsymbol{p}^*$ points at

$$\boldsymbol{\Delta} = \frac{\chi}{E_0} l(\cos\lambda, \sin\lambda). \tag{34}$$

A photon emitted with azimuthal angle ψ_1^* will hit the collimator at $\boldsymbol{r}_\gamma = \boldsymbol{\Delta} + \boldsymbol{k}_\perp + \boldsymbol{r}$, where

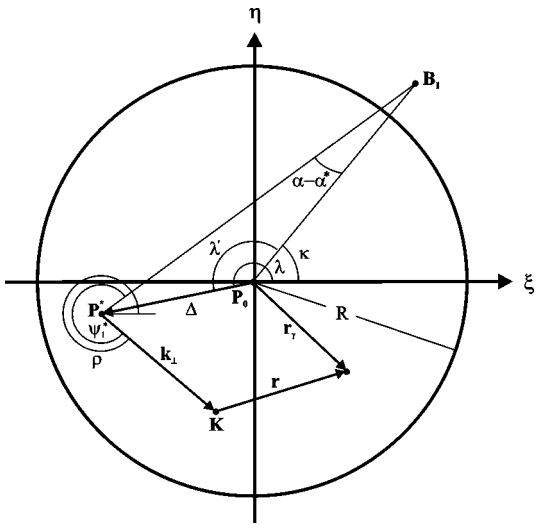

FIG. 3. The figure shows the photon collimator with radius R. The points B_1, P_0, P^*, and K denote the intersection point of the corresponding vectors $\mathbf{b}_1$, $\mathbf{p}_0$, $\mathbf{p}^*$, and $\mathbf{k}$ viewed along the direction $-\mathbf{p}_0$. Since all polar angles between the latter vectors are small, the angle between $\overline{B_1P_0}$ and $\overline{B_1P^*}$ can be approximated by $\alpha-\alpha^*$. The photon hits the collimator plane at $\mathbf{r}_\gamma = \boldsymbol{\Delta} + \mathbf{k}_\perp + \mathbf{r}$, with all vectors lying in the collimator plane and taking into account the divergence of the incident electron beam, the polar emission angle of the photon, and the lateral displacement, with respect to the beam axis, of the electron in the radiator, respectively.

$$\boldsymbol{k}_\perp = \frac{U^*(\psi_1^*,\chi,\lambda')}{E_0} l(\cos\rho, \sin\rho) \tag{35}$$

and, assuming small polar angles,

$$\rho = \psi_1^* + [\alpha^*(\chi,\lambda') - \alpha] + \kappa. \tag{36}$$

In order to obtain the cross section $d\sigma_R^{(c)}$ of coherent radiation observed behind a collimator of radius R we have to do a fivefold integration of Eq. (31), weighted with Eqs. (23) and (20), over ψ_1^*, χ, λ, ξ, and η, with the constraint $r_\gamma \leqslant R$:

$$\frac{d\sigma_R^{(c)}}{dk} = \int_{r_\gamma \leqslant R} K(\xi,\eta)\,d\xi\,d\eta\,P_{\rm res}(\chi,\lambda) \times \frac{d^2\sigma_\perp(\chi,\lambda-\kappa) + d^2\sigma_\parallel(\chi,\lambda-\kappa)}{d\psi_1^* dk} d\psi_1^*\chi\,d\chi\,d\lambda. \tag{37}$$

In the same way we get, by integration of Eq. (32),

$$\frac{d\sigma_{\perp R}^{(c)} - d\sigma_{\parallel R}^{(c)}}{dk} = \int_{r_\gamma \leqslant R} K(\xi,\eta)\,d\xi\,d\eta\,P_{\rm res}(\chi,\lambda) \times \frac{d^2\sigma_\perp(\chi,\lambda-\kappa) - d^2\sigma_\parallel(\chi,\lambda-\kappa)}{d\psi_1^* dk} \times d\psi_1^*\chi\,d\chi\,d\lambda. \tag{38}$$

If several reciprocal lattice vectors $\boldsymbol{g}$ lie in the pancake, the respective integrals in Eqs. (37) and (38) have to be summed.

At the fractional photon energy x the relative intensity of the photon beam behind the collimator is given by

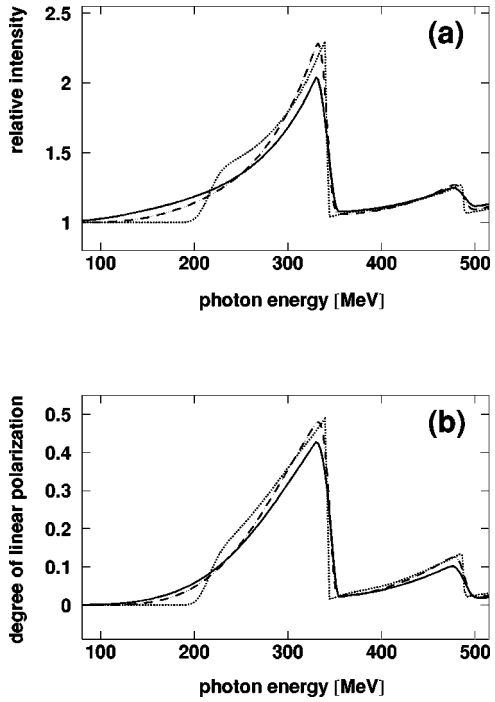

FIG. 4. Spectra of relative intensity (a) and degree of linear polarization (b) for different values of the beam parameters: (1) $\sigma_{p_x}/E_0=\sigma_{p_y}/E_0=0.01$ μrad, $d=1$ μm, $\sigma_x=\sigma_y=1$ μm (dotted lines), (2) $\sigma_{p_x}/E_0=\sigma_{p_y}/E_0=0.2$ mrad (dashed lines), and (3) $\sigma_{p_x}/E_0=\sigma_{p_y}/E_0=0.5$ mrad (solid lines). In (2) and (3) the other parameters have been kept constant: $d=0.1$ mm, $\sigma_x=0.2$ mm, and $\sigma_y=0.06$ mm. Electron energy, orientation of the radiator, and temperature are the same as in Fig. 2.

$$I_R(x,\theta,\alpha)=1+\frac{d\sigma_R^{(c)}}{f_c(R)d\sigma^{(i)}} \tag{39}$$

and its degree of linear polarization by

$$P_R(x)=\frac{d\sigma_{\perp R}^{(c)}-d\sigma_{\parallel R}^{(c)}}{d\sigma_R^{(c)}+f_c(R)d\sigma^{(i)}}. \tag{40}$$

V. CALCULATIONS

The integrations in Eqs. (37) and (38) can only be performed numerically. As input parameters the code takes the electron energy E_0, the four standard deviations describing the divergence and lateral extension of the electron beam, the thickness and temperature of the diamond radiator, its orientation angles θ and α with respect to the beam axis and φ with respect to the horizontal plane in the laboratory, the distance l between the radiator and the photon collimator, and the radius R of the latter. It then calculates spectra of relative intensity and polarization, i.e., the relative intensity and the degree of linear polarization of the collimated photon beam, as functions of the photon energy k. In addition, the code calculates, for a chosen single value of k, these quantities differentially as functions of the Cartesian coordinates x_c and y_c of the points of traversal of the photons in the collimator plane.

In Figs. 2 and 4 typical results of the calculations are displayed. At the electron energy $E_0=855$ MeV the radiator is oriented such that the most prominent discontinuity, viz., for $\boldsymbol{g}=[02\bar{2}]$, in the photon spectrum is located at $k_d=342$ MeV. The small peaks at higher photon energies belong to other reciprocal vectors $\boldsymbol{g}$ and are of minor importance.

In Fig. 2 the input parameters were fixed except for the opening angle of the collimator. A very small divergence of the electron beam was chosen. For three different angles of collimation (each much larger than the mean angle of divergence of the electron beam) the spectra of relative intensity and linear polarization are shown. The effects of collimation are clearly visible: with decreasing collimation angle the width of the peak becomes smaller, and in the vicinity of the maximum both the relative intensity and the degree of linear polarization increase. In Fig. 4 the collimating angle was kept fixed, and the divergence of the electron beam was varied in order to demonstrate its influence on the spectra. These curves give an explanation for our experimental observation that above a certain beam divergence the low-energy cutoff disappears (see the Introduction).

Figure 5 shows examples of the differential distributions of the relative intensity and the degree of linear polarization in the plane of the collimator. Both the electron energy and the orientation of the radiator were the same as in Figs. 2 and 4; i.e., the discontinuity for $\boldsymbol{g}=[02\bar{2}]$ is located at $k_d=342$ MeV. In Figs. 5(a) and 5(c) both the divergence and the diameter of the electron beam were assumed to be negligibly small, viz., for the former $\sigma_{p_x}/E_0=\sigma_{p_y}/E_0=0.001$ mrad and for the latter $\sigma_x=\sigma_y=0.1$ μm. The thickness of the radiator was very small too ($d=0.01$ mm). The distributions were calculated for the photon energy $k=307$ MeV, i.e., 35 MeV below the discontinuity. Figure 5(a) shows the relative intensity. Its central part, resembling the shape of a bishop's mitre, is contributed by the reciprocal vector $\boldsymbol{g}=[02\bar{2}]$. The much smaller circular ridge at the outer edge of the figure is due to $\boldsymbol{g}=[04\bar{4}]$ whose discontinuity lies at a much higher photon energy [cf. Eq. (16)]. Figure 5(c) is the corresponding plot of the degree of linear polarization. The plots in Figs. 5(b) and 5(d) are analogous to Figs. 5(a) and 5(c). However, for the parameters associated with the quality of the electron beam values were assumed which are typical for the beam properties at MAMI (Mainz): $\sigma_x=0.2$ mm, $\sigma_y=0.06$ mm, $\sigma_{p_x}/E_0=\sigma_{p_y}/E_0=0.042$ mrad, and thickness of the radiator 0.1 mm. As expected, the distributions in Figs. 5(a) and 5(c) now appear strongly smeared out. Nevertheless, they still differ from simple radial distributions without azimuthal dependence.

Figure 6 is the same as Fig. 5 but for the photon energy $k=340$ MeV, i.e., very close to k_d. Here, the contribution of $\boldsymbol{g}=[02\bar{2}]$ both to the relative intensity and the linear polarization is concentrated close to the forward direction.

The absolute intensity of the collimated beam is obtained by converting the differential distribution of relative intensity to that of absolute intensity and integrating the latter one over the collimator opening. The degree of linear polarization of the collimated beam is the average of the corresponding differential distribution (weighted by that of absolute intensity) over the collimator opening.

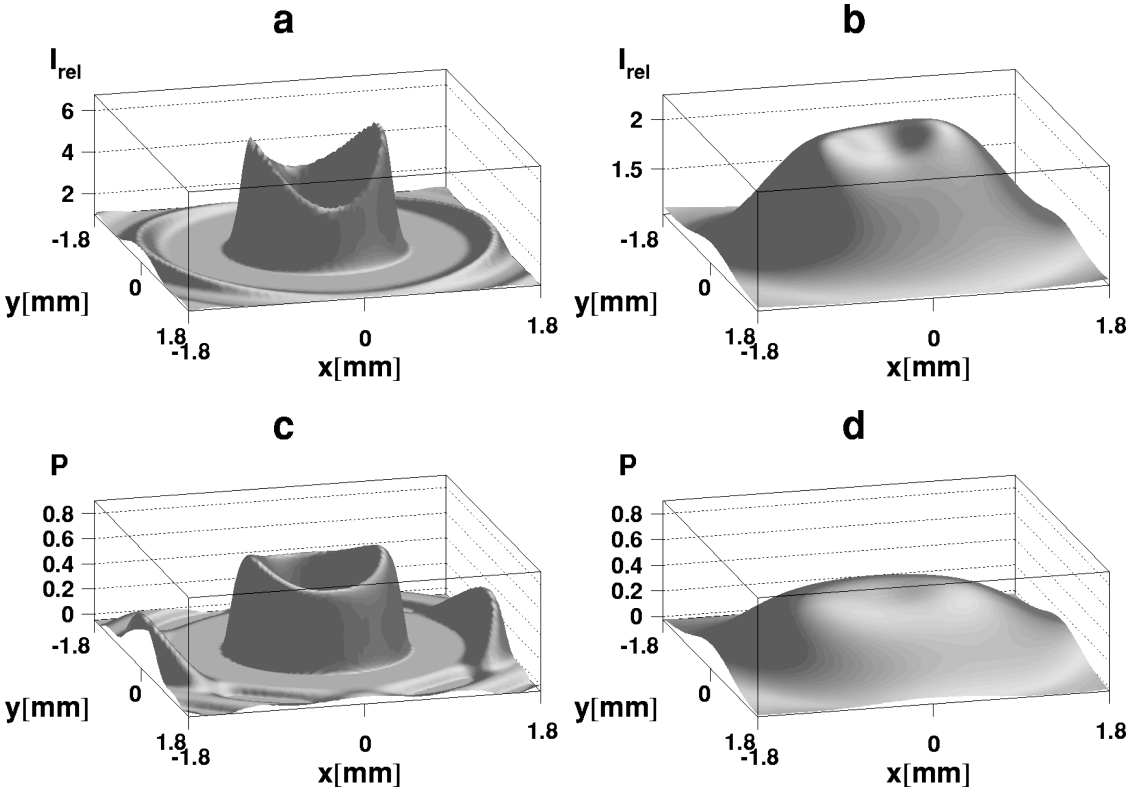

FIG. 5. Differential distributions of the relative intensity and of the degree of linear polarization of the photon beam in the collimator plane. The reference plane for the linear polarization is parallel to the horizontal plane of the laboratory, i.e., $\varphi=\pi/4$. The distributions are calculated for the photon energy $k=307$ MeV. (a) Relative intensity and (c) degree of linear polarization for a radiator of thickness $d=0.01$ mm and the electron beam parameters $\sigma_x=\sigma_y=0.1$ μm and $\sigma_{p_x}/E_0=\sigma_{p_y}/E_0=0.001$ mrad. (b) and (d) The same quantities for a radiator of thickness $d=0.1$ mm and electron beam parameters $\sigma_x=0.2$ mm, $\sigma_y=0.06$ mm, and $\sigma_{p_x}/E_0=\sigma_{p_y}/E_0=0.042$ mrad.

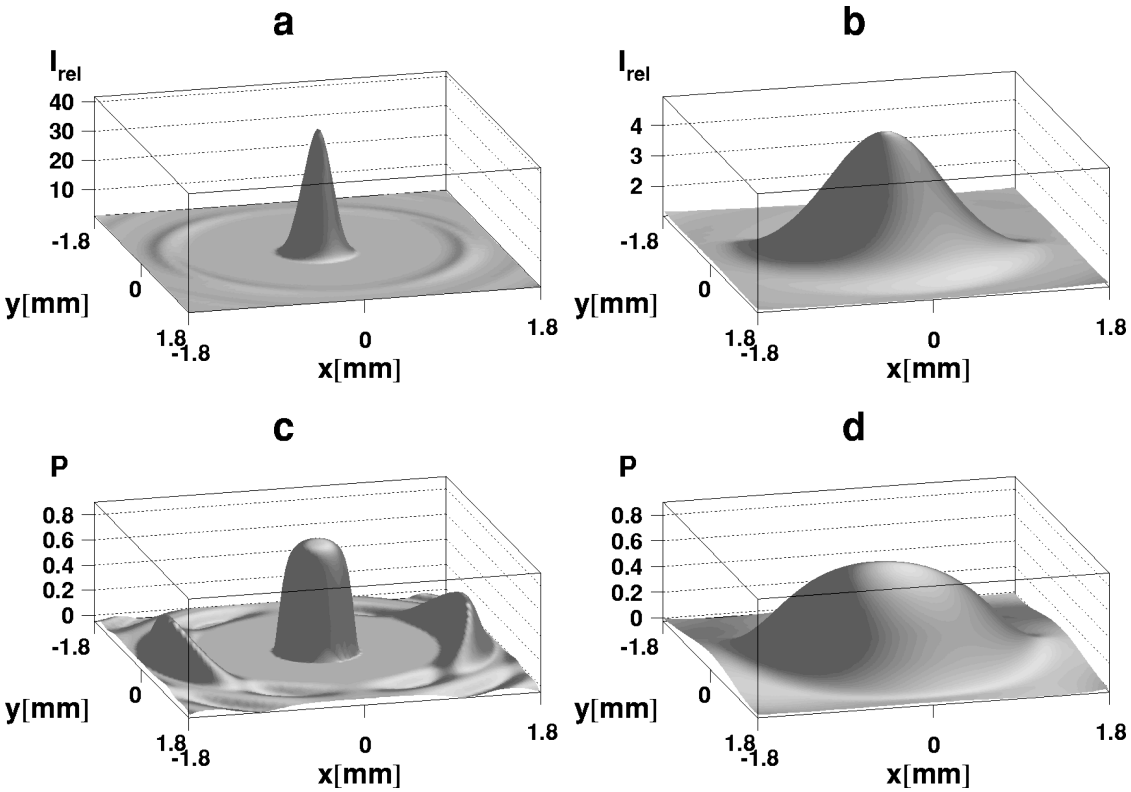

FIG. 6. Same distributions as in Fig. 5 but calculated for the photon energy $k=340$ MeV.

VI. MEASUREMENT OF LINEAR POLARIZATION

A photon polarimeter is characterized by its analyzing power K which is defined as

$$K=\frac{N^{\parallel}-N^{\perp}}{N^{\parallel}+N^{\perp}}. \tag{41}$$

Here $N^{\parallel}$ and $N^{\perp}$ are the counting rates obtained with the plane of polarization of a completely polarized photon beam being parallel and vertical, respectively, to the reference direction of the polarimeter.

In the present experiment the coherent photoproduction of π^0 mesons on ^{4}He nuclei served as the polarimeter reaction. Both the ^{4}He target and the π^0 product are spinless objects. Therefore, the information regarding the linear polarization of the photon beam is transferred completely to the azimuthal distribution of the emitted pions.

If the wave function of the photon is expanded into eigenstates of total angular momentum J and parity P_γ, we have, from conservation of angular momentum and parity,

$$P_\pi=(-1)(-1)^l=(-1)^{(J+1)}=P_\gamma, \tag{42}$$

where l and P_π denote the orbital angular momentum and the parity of the pion, respectively (the intrinsic parity of the π^0 is negative). Hence, coherent π^0 photoproduction on ^{4}He exclusively involves magnetic transitions. In the energy range of the present experiment the pions are emitted as p waves following $M1$ excitation of the Δ resonance. Denoting by $\boldsymbol{k}$ and k the momentum and energy of the incident photon, respectively, by $\boldsymbol{\epsilon}$ its polarization vector, by $\boldsymbol{q}_\pi$ the momentum of the emitted pion, and by $\boldsymbol{\rho}(k,\theta)$ the momentum transferred to the ^{4}He nucleus (all quantities referring to the center-of-mass system), the differential cross section of the process is

$$\begin{aligned}\frac{d\sigma}{d\Omega}(k,\theta_\pi,\phi)&=C(k)|(\boldsymbol{\epsilon}\times\hat{\boldsymbol{k}})\cdot\hat{\boldsymbol{q}}_\pi|^2|F(\rho)|^2\\&=C(k)\sin^2\theta_\pi\cos^2\phi|F(\rho)|^2\end{aligned} \tag{43}$$

where carets denote unit vectors, θ_π is the emission angle of the pion, and ϕ is the azimuthal angle between $\boldsymbol{\epsilon}$ and the normal to the $(\boldsymbol{q}_\pi,\boldsymbol{k})$ plane. $F(\rho)$ is the form factor of the nucleon distribution in ^{4}He. $C(k)$ is a normalization factor which does not depend on θ_π:

$$C(k)=\sigma^{\mathrm{tot}}(k)\Big/\left[\pi\int\sin^3\theta_\pi|F(k,\theta_\pi)|^2d\theta_\pi\right], \tag{44}$$

with $\sigma^{\mathrm{tot}}(k)$ denoting the total cross section for coherent pion photoproduction on ^{4}He. The asymmetry of the azimuthal distribution of the pion is

$$A=\frac{d\sigma/d\Omega^{(\phi=0)}-d\sigma/d\Omega^{(\phi=\pi/2)}}{d\sigma/d\Omega^{(\phi=0)}+d\sigma/d\Omega^{(\phi=\pi/2)}}=1. \tag{45}$$

The asymmetry A is identical to the analyzing power K of a hypothetical polarimeter in which the π^0 mesons are detected with perfect azimuthal resolution. For a real polarimeter, however, the analyzing power K depends on the method for detecting the π^0 mesons and its azimuthal resolution.

The π^0 meson decays with a probability of 0.99 into two photons which, in its rest frame, are emitted isotropically with equal energies but antiparallel directions. In the laboratory system there is a minimum angle $\alpha_{\min}$ between the directions of the two photons, viz.,

$$\alpha_{\min}=\arccos(1-2[m_\pi/E_\pi]^2), \tag{46}$$

where E_π and m_π are the total and rest energies of the pion, respectively. The laboratory energy ω_1 of one photon is a function of its emission angle α_1 with respect to the pion momentum:

$$\omega_1=\frac{m_\pi^2}{2(E_\pi-q_\pi\cos\,\alpha_1)}, \tag{47}$$

with its upper limit $\omega_1^{\max}=(E_\pi+q_\pi)/2$ corresponding to $\alpha_1=0$, i.e., forward emission of the photon. In the present experiment the π^0 meson was detected via one of its decay photons with an energy close to $\omega_1^{\max}$. The minimum angle $\alpha_{\min}$ from Eq. (46) prevents the detector from registering both decay photons of one pion and summing up their energies.

A competing reaction is the incoherent photoproduction of π^0 mesons on ^{4}He via formation of an excited state and subsequent disintegration of the target nucleus. It differs in two respects from the coherent reaction, favoring its experimental separation from the latter: (i) The first three incoherent channels have energy thresholds lying 21, 22, and 25 MeV, respectively, above that for the coherent reaction. Therefore, the pion decay photons have energies which are lower by at least 20 MeV than those from coherent photoproduction. (ii) The kinematics is closer to that of photoproduction on free nucleons than to that of coherent photoproduction on ^{4}He. Hence, the angular distribution of pions, in contrast to Eq. (43), does not contain the form factor of ^{4}He and, due to this, is shifted to larger angles.

The experiment was performed at MAMI (Mainz) [16,17] using the Glasgow tagged-photon facility [18,19]. Bremsstrahlung was produced by 855 MeV electrons in a diamond monocrystal of 100 μm thickness mounted on a three-axis goniometer. A detailed description of the goniometer and of the technique used for orienting the radiator is given in Ref. [1]. The collimator was made of lead 10 cm thick and had a radius R of either 1.75 or 1.25 mm, corresponding to collimating angles Θ_c of 0.7 and 0.5 mrad, respectively. The characteristic angle of incoherent bremsstrahlung was $\Theta_{\mathrm{BH}}=0.6$ mrad.

The polarimeter setup is identical to the apparatus described in Ref. [20]. It consisted of a liquid He target and the large Mainz 48 cm diameter$\times$64 cm modular NaI(Tl) detector positioned at the laboratory angle $\theta_{\mathrm{lab}}=37°$. This angle is close to the maximum of the angular distribution of π^0 mesons from coherent photoproduction on ^{4}He at photon energies around 300 MeV. The angular distribution of pions from incoherent photoproduction has its maximum at considerably larger angles. A lead collimator of 13.8 cm diameter at a distance of 83 cm from the ^{4}He target defined a solid angle of 22 msr. The energy resolution of the detector was 1.5%. It

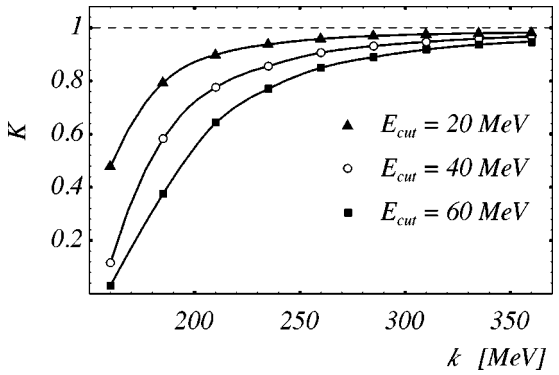

FIG. 7. Analyzing power K of the polarimeter as a function of the photon energy k calculated using the simulation code GEANT. E_{cut} is the width of the energy interval chosen for determining the number of photons from pion decay (see text for details).

is sufficient to separate, in the energy region of interest, decay photons of π^0 mesons from photons scattered elastically by ^{4}He into the detector.

The analyzing power K of the polarimeter setup was calculated as a function of the incident photon energy k using the simulation code GEANT [21]. The simulation takes into account (i) the kinematics of the coherent π^0 production on ^{4}He and of the subsequent pion decay, including the angular distribution of the pions, (ii) the geometry of the apparatus, and (iii) the response of the NaI detector to photons.

At fixed k the continuous decay photon spectra registered by the NaI detector were simulated for completely polarized incident photons having, alternatively, vertical (v) and horizontal (h) orientation of the electric vector. For displaying the spectra the ''missing energy'' $E_{\mathrm{miss}}=E_{\mathrm{coh}}-\omega_1$ is used where E_{coh} is the energy of photons scattered elastically by ^{4}He nuclei into the detector. On the E_{miss} scale the decay photon spectrum has a lower limit E_0 depending on k. Intervals of width E_{cut} starting at E_0 were selected in both spectra, and the normalized numbers N_{v} and N_{h} of simulated events in the energy intervals were used for calculating the analyzing power $K=(N_{\mathrm{v}}-N_{\mathrm{h}})/(N_{\mathrm{v}}+N_{\mathrm{h}})$. Figure 7 shows the analyzing power K determined by the simulation as a function of the incident photon energy and for different values of the interval width E_{cut}. The dependence of K on E_{cut} can be understood from Eq. (47) which shows that a lower limit for the energy of detected decay photons corresponds to an upper limit for the angle α_1 and, therefore, determines the effective angular resolution of the polarimeter setup for the π^0 mesons. At incident photon energies above 250 MeV the analyzing power is larger than 0.9 for $E_{\mathrm{cut}}=20$ MeV where pion photoproduction is purely coherent and larger than 0.8 for any $E_{\mathrm{cut}}\leqslant 60$ MeV without, however, considering incoherent pion photoproduction.

The linear polarization of the collimated bremsstrahlung beam was measured as a function of photon energy k by taking, in coincidence with the tagger detectors, photon spectra of the NaI detector. The radiator crystal was oriented such that the prominent discontinuity corresponding to the reciprocal vector $\boldsymbol{g}=[02\bar{2}]$ was located at $k_d=320$ MeV. The plane of polarization was either vertical or horizontal in the laboratory, and was interchanged regularly during the measurements by suitably changing the orientation of the diamond radiator. As an example, Fig. 8 shows spectra measured for the incident photon energy $k=306$ MeV which is close to the maximum of linear polarization. They are normalized to the same number of incident photons. In both spectra there is a clear separation between coherently scattered photons centered at $E_{\mathrm{miss}}=0$ and the continuum of photons from π^0 decay starting at $E_0\approx 12$ MeV. The hatched areas in both spectra mark intervals of equal width E_{cut} placed on the continuum, yielding the photon numbers I_{v} and I_{h} from which the degree of linear polarization is determined via

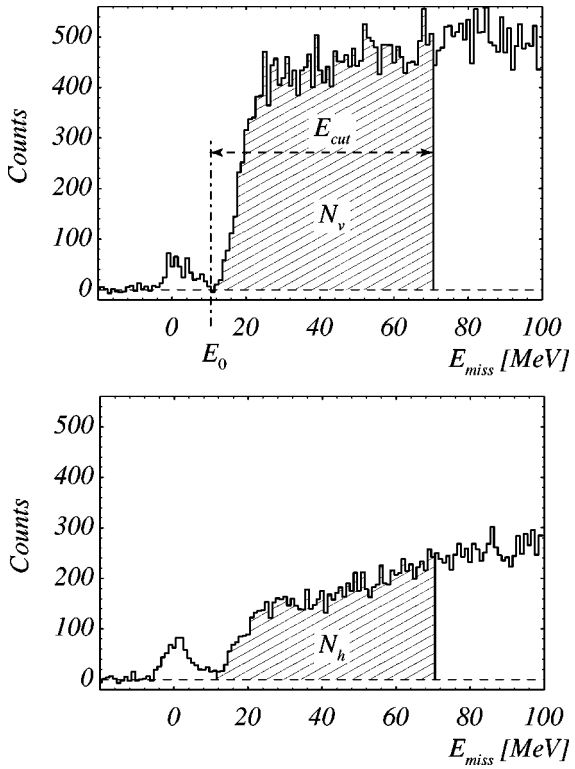

FIG. 8. Normalized spectra of photons measured for the collimation angle $\Theta_{\mathrm{c}}=0.7$ mrad at the incident photon energy $k=306$ MeV. The diamond radiator was oriented such that the discontinuity corresponding to the reciprocal vector $\boldsymbol{g}=[02\bar{2}]$ was located at $k_{\mathrm{d}}=320$ MeV. The plane of polarization of the incident photons was oriented either vertically (upper half) or horizontally (lower half) in the laboratory. The abscissa is the energy difference $E_{\mathrm{miss}}=E_{\mathrm{coh}}-\omega_1$ with E_{coh} being the energy of incident photons scattered coherently by ^{4}He nuclei into the detector and ω_1 the photon energy. The hatched areas of width E_{cut} were used for determining the number of photons I_{v} and I_{h}, respectively, which yield the degree of polarization. E_{cut} was varied between 20 and 60 MeV.

$$P=\frac{1}{K}\frac{I_{\mathrm{v}}-I_{\mathrm{h}}}{I_{\mathrm{v}}+I_{\mathrm{h}}}, \tag{48}$$

with K being the analyzing power of the polarimeter.

The degree of linear polarization was determined from the spectra for different values of E_{cut} ranging from 20 to 60 MeV. At $E_{\mathrm{cut}}=20$ MeV, Eq. (48) yields the true value of P because only coherent π^0 photoproduction is utilized. With $E_{\mathrm{cut}}>20$ MeV, however, incoherent photoproduction might contribute. With E_{cut} being gradually shifted from 20 to 60 MeV an almost linear decrease of the apparent degree of

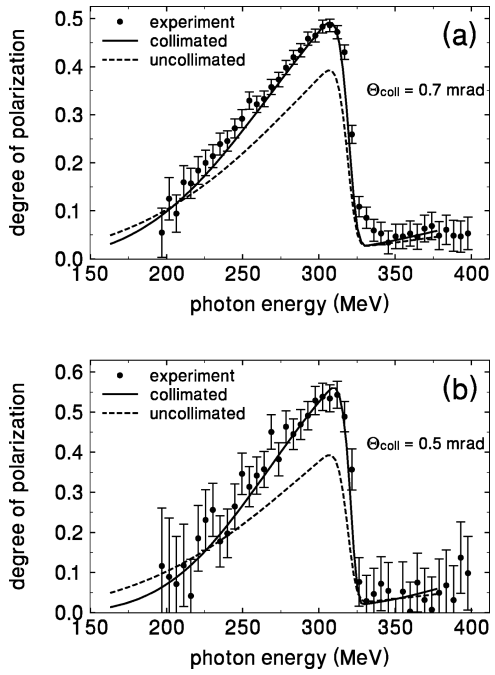

FIG. 9. Degree of linear polarization of collimated coherent bremsstrahlung measured through the beam asymmetry of coherent π^0 photoproduction. Solid curve: calculated for the actual collimator having (a) $\Theta_c=0.7$ mrad and (b) $\Theta_c=0.5$ mrad. Dash-dotted curves: calculated for the case of no collimation.

polarization, amounting to 7% at $E_{\rm cut}=60$ MeV, was observed. By using this empirical correction obtained from the spectra measured for $\Theta_c=0.7$ mrad the statistical accuracy in the evaluation of P for $\Theta_c=0.5$ mrad could be improved.

A preliminary account of the experiment is given in Ref. [10]. Figures 9(a) and 9(b), taken from that paper, show the measured degree of linear polarization, together with that calculated using the theory developed in the present paper, for the two collimators mentioned above. The agreement between measured and calculated values is excellent. In addition, the polarization is calculated for an uncollimated photon beam. The enhancement of the linear polarization by collimation of the photon beam is clearly demonstrated. Furthermore, Fig. 10 shows typical spectra of relative intensities obtained using the $R=1.25$ mm collimator for two different orientations of the crystal and the corresponding calculated spectra. Again, the calculated spectra agree excellently with the measured data.

VII. CONCLUSION

The spectrum and the linear polarization of coherent bremsstrahlung produced by extremely relativistic electrons on a diamond monocrystal can be calculated for an electron beam having a lateral extension as well as an angular divergence. Results of the calculation are compared to those of an experiment using the tagged bremsstrahlung facility at the electron accelerator MAMI (Mainz), in which a polarimeter based on coherent π^0 meson photoproduction on ^{4}He nuclei was used. Excellent agreement between measured and calculated quantities is observed. On the basis of this result the degree of linear polarization can be determined, without using a polarimeter, by fitting the beam parameters to an observed spectrum of relative intensity and, after that, applying Eq. (40). From this procedure a simplified method can be derived which directly transforms the spectrum of relative intensity to that of linear polarization.

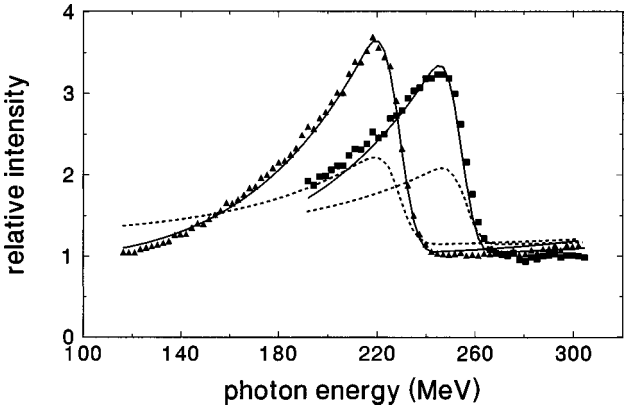

FIG. 10. Relative intensity of collimated coherent bremsstrahlung for two different orientations of the diamond crystal measured through a coincidence arrangement using the tagger and a lead glass detector in direct beam. Solid curves: calculated for the actual collimator having $\Theta_c=0.5$ mrad. Dashed curves: calculated for the case of no collimation.

ACKNOWLEDGMENTS

This work was supported by Deutsche Forschungsgemeinschaft (SFB 201 and Schu 222). The authors wish to thank Dr. J. P. Capitani for providing a copy of Ref. [14] and Dr. P. Grabmayr for his interest in this work.

APPENDIX

For the convenience of the reader we collect all planes and angles we used to explain the theory in Fig. 11 and Tables I and II. In addition, the Φ and Ψ functions used in Sec. III are collected. They were taken from Refs. [14,2,11]. In the following, the summations run only over those vectors $\boldsymbol{g}$ of the reciprocal lattice which lie in the pancake, i.e., for which U from Eq. (10) is real:

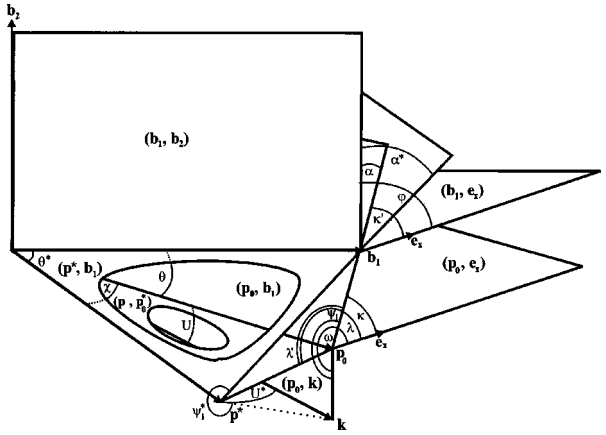

FIG. 11. Kinematics of coherent bremsstrahlung under experimental conditions. From the figure we see that $\lambda=\lambda'+\kappa$, $\omega=\psi_1+\kappa$, and $\varphi=\alpha+\kappa'$. If we assume $\theta\ll 1$, we have $\kappa\approx\kappa'$ and, therefore, $\omega=\psi_1+\varphi-\alpha$.

TABLE I. Definition of all planes used in the theory (cf. Fig. 11).

Definition	Denotation
$(\mathbf{b}_1,\mathbf{b}_2)$	crystal plane
$(\mathbf{p}_0,\mathbf{b}_1)$	plane of incidence
$(\mathbf{p}_0,\mathbf{k})$	plane of emission
$(\mathbf{p}_0,\mathbf{q})$	recoil plane
$(\mathbf{b}_1,\mathbf{e}_x)$	reference plane
$(\mathbf{p}_0,\mathbf{e}_x)$	horizontal plane of the laboratory
$(\mathbf{p}_0,\mathbf{p}^*)$	plane of divergence
$(\mathbf{p}^*,\mathbf{b}_1)$	—

$$\Phi_1(\delta,\theta,\alpha)=\frac{8\pi}{N_0a^3}\sum_{\boldsymbol{g}}\ |S(\boldsymbol{g})|^2\frac{F^2(g^2)}{g^4}e^{-Ag^2}\frac{\delta g_{\mathrm{t}}^2}{g_{\mathrm{l}}^2(\theta,\alpha)},$$

$$\Phi_2(\psi_1,\delta,\theta,\alpha)=\frac{96\pi}{N_0a^3}\sum_{\boldsymbol{g}}\ |S(\boldsymbol{g})|^2\frac{F^2(g^2)}{g^4}\times e^{-Ag^2}\Gamma^2(\psi_1,\alpha)\Lambda(\delta,\theta,\alpha),$$

$$\Phi_4(\psi_1,\delta,\theta,\alpha)=\frac{8\pi}{N_0a^3}\sum_{\boldsymbol{g}}\ |S(\boldsymbol{g})|^2\frac{F^2(g^2)}{g^4}\,e^{-Ag^2}\times\left\{\frac{\delta\Upsilon(\varphi)}{g_{\mathrm{l}}^2(\theta,\alpha)}-4\cos 2(\psi_1+\varphi-\alpha)\times\Gamma^2(\psi_1,\alpha)\Lambda(\delta,\theta,\alpha)-2\sin\times 2[(\psi_1+\varphi-\alpha)]\Delta(\psi_1,\alpha)\frac{\delta(g_{\mathrm{l}}(\theta,\alpha)-\delta)}{g_{\mathrm{l}}^3(\theta,\alpha)}\right\},$$

$$\Psi_1^{(\mathrm{i})}=4+4\int_\delta^1(1-e^{-Aq^2})\frac{F^2(q^2)}{q^4}(q-\delta)^2q\ dq,$$

$$\Psi_2^{(\mathrm{i})}=\frac{10}{3}+4\int_\delta^1(1-e^{-Aq^2})\frac{F^2(q^2)}{q^4}\times\left(q^2-6\delta^2\ln\frac{q}{\delta}+3\delta^3-4\frac{\delta^3}{q}\right)q\ dq.$$

The quantities $\Psi_1^e=4.05$ and $\Psi_2^e=3.94$ are corrections due to contributions by the electrons in the carbon atom [22]:

$$\Psi_1^{(\mathrm{c})}(\delta,\theta,\alpha)=4\frac{(2\pi)^2}{a^3}\frac{1}{N_0}\times\sum_{\boldsymbol{g}}\ |S(\boldsymbol{g})|^2\frac{F^2(g^2)}{g^4}e^{-Ag^2}\frac{\delta g_{\mathrm{t}}^2}{g_{\mathrm{l}}^2(\theta,\alpha)},$$

TABLE II. Definition of all angles used in the theory (cf. Figs. 3 and 11).

Polar angles			Azimuthal angles	
Symbol		Definition	Symbol	Definition
[rad]	$[1/E_0]$		[rad]	
Θ_k	U	$\angle(\mathbf{p}_0,\mathbf{k})$	α	$\angle(\mathbf{p}_0,\mathbf{b}_1),(\mathbf{b}_1,\mathbf{b}_2)$
—	U^*	$\angle(\mathbf{p}^*,\mathbf{k})$	α^*	$\angle(\mathbf{p}^*,\mathbf{b}_1),(\mathbf{b}_1,\mathbf{b}_2)$
θ	ϑ	$\angle(\mathbf{p}_0,\mathbf{b}_1)$	ψ_1	$\angle(\mathbf{p}_0,\mathbf{k}),(\mathbf{p}_0,\mathbf{b}_1)$
θ^*	ϑ^*	$\angle(\mathbf{p}^*,\mathbf{b}_1)$	ψ_1^*	$\angle(\mathbf{p}^*,\mathbf{k}),(\mathbf{p}^*,\mathbf{b}_1)$
—	χ	$\angle(\mathbf{p}_0,\mathbf{p}^*)$	ω	$\angle(\mathbf{p}_0,\mathbf{k}),(\mathbf{p}_0,\mathbf{e}_x)$
			φ	$\angle(\mathbf{b}_1,\mathbf{e}_x),(\mathbf{b}_1,\mathbf{b}_2)$
			κ	$\angle(\mathbf{p}_0,\mathbf{b}_1),(\mathbf{p}_0,\mathbf{e}_x)$
			κ'	$\angle(\mathbf{p}_0,\mathbf{b}_1),(\mathbf{b}_1,\mathbf{e}_x)$
			λ	$\angle(\mathbf{p}_0,\mathbf{p}^*),(\mathbf{p}_0,\mathbf{e}_x)$
			λ'	$\angle(\mathbf{p}_0,\mathbf{p}^*),(\mathbf{p}_0,\mathbf{b}_1)$

$$\Psi_2^{(\mathrm{c})}(\delta,\theta,\alpha)=24\frac{(2\pi)^2}{a^3}\frac{1}{N_0}\sum_{\boldsymbol{g}}\ |S(\boldsymbol{g})|^2\times\frac{F^2(g^2)}{g^4}e^{-Ag^2}g_{\mathrm{t}}^2\Lambda(\delta,\theta,\alpha),$$

$$\Psi_3^{(\mathrm{c})}(\delta,\theta,\alpha)=-4\frac{(2\pi)^2}{a^3}\frac{1}{N_0}\times\sum_{\boldsymbol{g}}\ |S(\boldsymbol{g})|^2\frac{F^2(g^2)}{g^4}e^{-Ag^2}\frac{\delta^3\Upsilon(\varphi)}{g_{\mathrm{l}}^4(\theta,\alpha)}.$$

In these definitions N_0 is the number of atoms in the unit cell, a^3 the volume of the unit cell, $F(q^2)=1-F'(q^2)$ where $F'(q^2)$ is the atomic form factor for photon scattering, $S(\boldsymbol{g})$ is the structure factor, and e^{-Ag^2} the Debye-Waller factor. The remaining quantities are

$$\Gamma(\psi_1,\alpha)=-g_2\cos(\psi_1-\alpha)+g_3\sin(\psi_1-\alpha),$$

$$\Lambda(\delta,\theta,\alpha)=\frac{\delta^2(g_{\mathrm{l}}(\theta,\alpha)-\delta)}{g_{\mathrm{l}}^4(\theta,\alpha)},$$

$$\Delta(\psi_1,\alpha)=(g_2^2-g_3^2)\sin(2\psi_1-2\alpha)+2g_2g_3\cos(2\psi_1-2\alpha),$$

$$\Upsilon(\varphi)=(g_2^2-g_3^2)\cos 2\varphi+2g_2g_3\sin 2\varphi.$$

[1] D. Lohmann *et al.*, Nucl. Instrum. Methods Phys. Res. A **343**, 494 (1994).
[2] H. A. Bethe and W. Heitler, Proc. R. Soc. London, Ser. A **146**, 83 (1934).
[3] R. F. Mozley and J. DeWire, Nuovo Cimento **27**, 1281 (1963).
[4] S. Kato, T. Kifune, Y. Kimura, M. Kobayashi, K. Kondo, T. Nishikawa, H. Sasaki, K. Kikuta, and K. Kohva, J. Phys. Soc. Jpn. **20**, 303 (1965).
[5] L. Criegee, M. Garrell, H. Sadrozinski, U. Timm, and W. Zimmermann, Phys. Lett. **28B**, 140 (1968).
[6] T. Tsuru, S. Kurokawa, T. Nishikawa, S. Suzuki, T. Katayama, M. Kobayashi, and K. Kondo, Phys. Rev. Lett. **27**, 609 (1971).
[7] W. Kaune, G. Miller, W. Oliver, R. W. Williams, and K. K. Young, Phys. Rev. D **11**, 478 (1975).
[8] G. Lutz, Nuovo Cimento A **53**, 242 (1968).
[9] U. Timm, Fortschr. Phys. **17**, 765 (1969).
[10] A. Kraus *et al.*, Phys. Rev. Lett. **79**, 3834 (1997).
[11] G. Diambrini-Palazzi, Rev. Mod. Phys. **40**, 611 (1968).
[12] A. W. Saénz and H. Überall, *Coherent Radiation Sources* (Springer, Berlin, 1985).
[13] M. M. May, Phys. Rev. **84**, 265 (1951).
[14] G. Barbiellini, G. Bologna, G. Diambrini, and G. P. Murtas, Laboratori Nazionali di Frascati Report No. LNF-62/114, 1962 (unpublished).
[15] H. A. Bethe and J. Ashkin, in *Experimental Nuclear Physics*, edited by E. Segrè (Wiley, New York, 1953), Vol. I, Secs. D–E, p. 166.
[16] H. Herminghaus, A. Feder, K. H. Kaiser, W. Manz, and H. v.d. Schmitt, Nucl. Instrum. Methods **138**, 1 (1976).
[17] H. Herminghaus, K. H. Kaiser, and U. Ludwig, Nucl. Instrum. Methods Phys. Res. A **187**, 103 (1981).
[18] I. Anthony, J. D. Kellie, S. J. Miller, and J. Ahrens, Nucl. Instrum. Methods Phys. Res. A **301**, 230 (1991).
[19] S. J. Hall, G. J. Miller, R. Beck, and P. Jennewein, Nucl. Instrum. Methods Phys. Res. A **368**, 698 (1996).
[20] O. Selke *et al.*, Phys. Lett. B **369**, 207 (1996).
[21] R. Brun *et al.*, GEANT simulation code, version 3.16, CERN Report No. DD/EE/84-1, 1987.
[22] J. A. Wheeler and W. E. Lamb, Phys. Rev. **55**, 858 (1939).